

## Supporting Information for: Topological Winding Number Change and Broken Inversion Symmetry in a Hofstadter's Butterfly

Peng Wang,<sup>1</sup> Bin Cheng,<sup>1</sup> Oleg Martynov,<sup>1</sup> Tengfei Miao,<sup>1</sup> Lei Jing,<sup>1\*</sup> Takashi Taniguchi,<sup>2</sup> Kenji Watanabe,<sup>2</sup> Vivek Aji,<sup>1</sup> Chun Ning Lau,<sup>1</sup> Marc Bockrath<sup>1†</sup>

<sup>1</sup>Department of Physics and Astronomy, University of California, Riverside, California 92521, USA.

<sup>2</sup>Advanced Materials Laboratory, National Institute for Materials Science, Tsukuba, Ibaraki 305-0044, Japan.

\*Present address: Applied Materials, Inc., 3330 Scott Blvd, M/S 0606, Santa Clara, CA, 95054, USA.

†E-mail: marc.bockrath@ucr.edu

### S1. Sample Fabrication

Samples are fabricated by placing graphene on hBN using Elvacite 2550 layers,<sup>1</sup> on top of an oxidized Si wafer with 300 nm oxide. The doped Si acts as a back gate. The edges' cleavage planes are oriented to within approximately  $\sim 1^\circ$  under an optical microscope.<sup>2-4</sup> Raman measurements are used to verify the lattice alignment,<sup>5,6</sup> and electrodes are attached using electron-beam lithography.

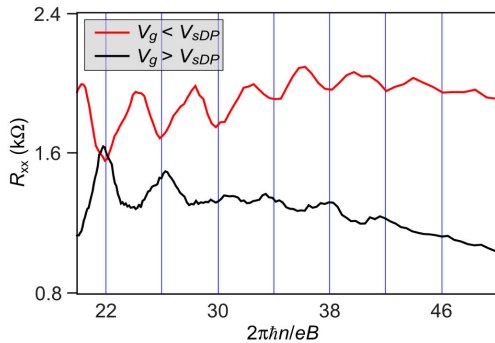


**Figure S1. Magnetooscillation data for sample G1.** Plot of  $R_{xx}$  vs. filling factor  $\nu=2\pi n\hbar/eB$ , for electron density below the sDP (red),  $V_g=40$  V, and above (black),  $V_g=72.4$  V.

$\pm 4$ , consistent with previous studies.<sup>2-4</sup> For the three samples we find  $n_0=0.81 \times 10^{12}$  cm<sup>-2</sup> for G1,  $0.58 \times 10^{12}$  cm<sup>-2</sup> for G2, and  $0.64 \times 10^{12}$  cm<sup>-2</sup> for G3. From the normalized density, the area of the moiré unit cell  $1/n_0$  is used to determine the normalized magnetic field  $\phi/\phi_0$ , which is the number of flux quanta per superlattice unit cell.

### S2. Parameter Normalization

To plot the data in terms of  $n/n_0$ , we determined  $n$  by measuring the Shubnikov-de Haas oscillations in  $R_{xx}$  at low  $B$  field using a range of densities near the secondary Dirac point. The density  $n_0$ , which corresponds to one electron per superlattice unit cell, was then extracted from the oscillations in  $R_{xy}$  that are independent of gate voltage near the secondary Dirac point called “Zak oscillations.”<sup>4</sup> Contours of these are shown by the black dashed lines in Fig. 2b of the main text. This enables the normalized density  $n/n_0$  to be computed, which can be determined for the extrapolation point to  $B=0$  of the Landau fan features from the secondary Dirac Point (sDP). These occur at  $n/n_0 =$

### S3. Magnetooscillation data for sample G1

Figure S1 shows magnetooscillations at constant density versus filling factor from sample G1 taken at a gate voltage above the sDP ( $V_g=72.4$  V) in black, and from below ( $V_g=40$  V) in red. The two curves show a  $\pi$  phase shift. The curves are presented without background subtraction.

### S4. Two-terminal magnetotransport data for sample G2

We show in Fig. S2 magnetotransport data for a two-terminal aligned device G2 that exhibits secondary Dirac point features. The graphene/h-BN alignment was confirmed by Raman spectroscopy.<sup>5,6</sup> Figure S2a plots the two-terminal conductance versus  $B$  and  $V_g$ . Following the Landau fan features corresponding to a conductance minimum along constant filling factor  $\nu$  (for example along the black dashed line) originating from the main Dirac Point (mDP), the

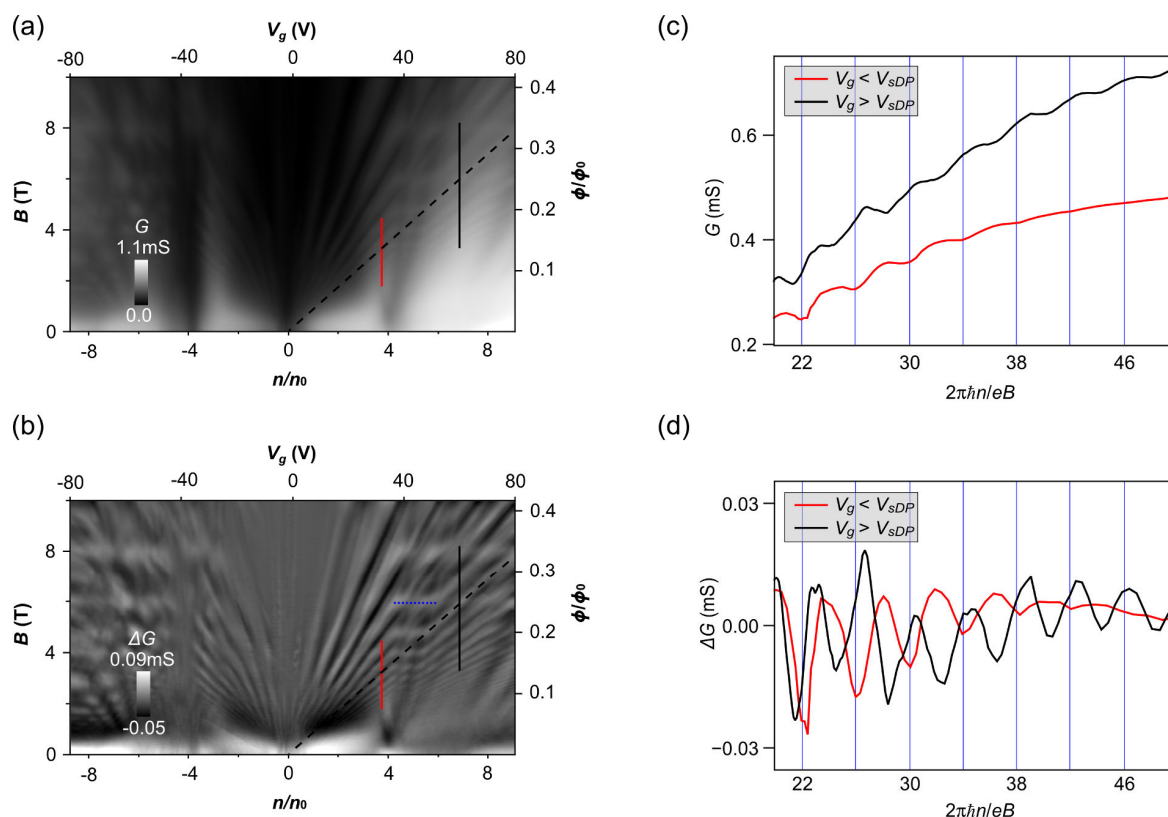


**Figure S2. Data for sample G2.** (a) Gray scale of  $G$  vs. gate voltage (top axis)/normalized charge density (bottom axis) and  $B$  (left axis)/flux quanta per unit moiré superlattice unit cell (right axis). (b) Gray scale of background subtracted  $G$  ( $\Delta G$ ) with the same axes as in (a). (c) Plot of  $G$  vs. filling factor  $\nu=2\pi n\hbar/eB$ , for electron density below the sDP (red) and above (black). (d) Plot of  $\Delta G$  vs.  $\nu$  for electron density below the sDP (red) and above (black).

conductance makes a transition to a maximum upon crossing through the sDP at  $n/n_0=4$  on the electron doped side, indicating a  $\pi$  phase shift in the magneto-oscillations vs.  $\nu$ .

To improve the feature contrast, in Fig. S2b we plot the conductance with a smoothed background subtracted, labeled  $\Delta G$ . The transition in phase is visible as the flat features independent of gate voltage (Zak oscillations<sup>4</sup>), such as that shown by the blue dotted line. The transition region broadens as  $B$  increases, and is bounded by  $n/n_0 \approx 4$  and approximately by a relative filling factor  $\nu \sim 10$  on the right. These bands occur when the flux quanta per unit cell is  $1/q$ , where  $q$  is an integer, yielding particularly large gaps between states.<sup>2-4, 7, 8</sup> In the flat region, these gaps are presumably dominant, while outside the transition region, the conventional cyclotron gaps are dominant, although more work will be required to fully understand the behavior of the system within the transition region. However, we now focus on the behavior outside of the transition region where the Landau fan features are dominant. At low densities the features are somewhat irregular, and curve towards the density axis at the lowest densities. This may be due to a combination of quantum interference phenomena<sup>9</sup> and insufficiently screened charge puddles.<sup>10-12</sup> However, above  $n/n_0 \approx 2$ , the Landau fan features are relatively regular and follow approximately straight lines outside of the transition region. As the density is tuned through the transition region,  $\Delta G$  changes from a minimum to a maximum along lines of constant filling factor such as shown by the black dashed line. To confirm the phase shift we rely on quantitative analysis of the line traces given in the figures such as Fig. S2c-d [also in Fig. S3 (below) and Figs. 3a and 4 in the main text], which shows line traces vs. filling factor taken from

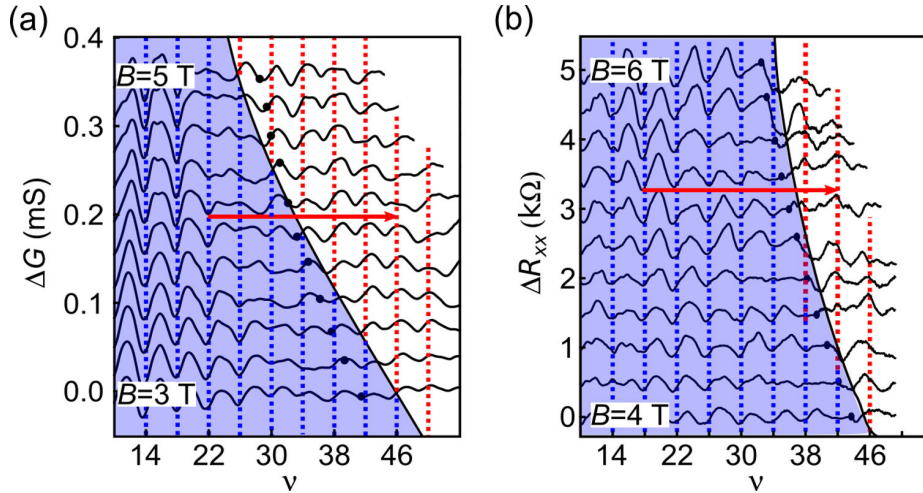


**Figure S3. Horizontal line traces for samples G2 and G1.** (a) Plot of  $\Delta G$  vs.  $\nu = 2\pi n\hbar/eB$ , for  $B$  ranging from 3 T to 5 T in 0.2 T increments for samples G2. Equally spaced dashed lines are drawn as a guide to the eye, where blue follows  $\Delta G$  minima and red follows the maxima. For each line trace, a black circle (marking a relative filling factor of approximately +10 from the sDP) is drawn indicating near where the phase shift in the oscillations with respect to  $\nu(V_g)$  occurs. The  $\pi$  Berry phase region is shaded blue, while the  $0 \bmod (2\pi)$  phase region is unshaded. (b) Plot of  $\Delta R_{xx}$  vs.  $\nu = 2\pi n\hbar/eB$ , for  $B$  ranging from 4 T to 6 T for sample G1. Dashed lines are drawn as guides to the eye as in (a), except blue follows  $\Delta R_{xx}$  minima and red follows  $\Delta R_{xx}$  maxima. Black circles and shaded/unshaded regions are as in (a). The vertical scale to the right of the black circles is expanded by a factor of 3.

Figs. S2a-b along the black and red lines. Figures S2c-d show that the background subtraction does not create any spurious or extra features in our data, as both figures with and without background subtraction show a similar transition of the magneto-oscillation phase, as the minima from the left of the sDP (red line) align with the maxima from the right of the sDP (black line).

### S5. Horizontal line traces showing the phase shift for sample G2 and G1

In order to further verify the presence of the  $\pi$  phase shift, we show here horizontal gate traces for G1 and G2. In Fig. S3a, we plot  $\Delta G$  vs.  $\nu$  for device G2 with  $B$  ranging from 3 T to 5 T. The phase shift occurs near  $n/n_0=4$ , at a relative filling factor  $\sim 10$  from the sDP that occurs just to the right of the Zak oscillation region; for each line trace, the approximate location of relative  $\nu=10$  is drawn as a black circle. To the left of the transition (blue shading) the period of the oscillations is 4 and the minima in  $\Delta G$  are aligned with the equally spaced vertical dashed lines. However, near the black circles, the phase starts to shift and a  $\pi$  shift is observed towards the right end of the traces (unshaded) where instead the maxima in  $\Delta G$  are aligned with the dashed lines. This is shown for example along the red arrow, which connects a minimum to a maximum across the  $\pi$  phase shift boundary. The observed phase shift in the gate traces is insensitive to offsets in the magnetic field since this would only affect the period but not the relative phase difference between the two regions (We find that by plotting in dimensionless units of the period as measured to the left of sDP where the phase offset is constant, a similar  $B$ -independent result is obtained). Moreover, a magnetic field offset would cause the phase shift to occur at lower values of filling factor for lower fields, while the opposite is observed in Fig. S3. We thus rule out magnetic field offsets as the origin of the observed phase shift behavior. Finally, the phase shift is also insensitive to charge offsets as these would shift the curves, but also not affect the relative phase difference between the two regions.

To perform a similar analysis on sample G1, we plot in Fig. S3b the background subtracted  $\Delta R_{xx}$  vs.  $\nu$  and expand the vertical scale to the right of the black circles by a factor of 3. A similar  $\pi$  phase shift is observed in the gate traces. To the left of the transition, the vertical dashed lines align with  $\Delta R_{xx}$  minima, and to the right of the transition they align to the  $\Delta R_{xx}$  maxima. This is shown by the red arrow, which connects a minimum to a maximum across the transition.

Finally, we note that for a given maximum magnetic field, a larger twist angle yields a larger density  $n_0$  at which the sDP features are observed and hence a larger filling factor would generally be expected to observe the phase shift, consistent with the behavior shown by samples G1 and G2.

### S6. Behavior under hole doping

For large hole density a distinctive pattern of hexagonal ridges in  $R_{xx}$  emerges in the plot of  $R_{xx}$  vs.  $B$  and  $V_g$ . This is shown in Fig. S4a for a third sample G3 in which the hexagonal features were more clearly resolved (a charge inhomogeneity precluded analysis of the phase shift for

electron doping in this sample). Measurement of  $R_{xy}$  shows a plateau at the minimum of the  $R_{xx}$  in the hexagon centers indicating the presence of a gap, as shown in Fig S4b. At  $B \approx 5$  T, the field corresponding to the Zak band at  $\phi/\phi_0 = 1/5$ , a third generation replica Dirac point<sup>3,4</sup> appears showing a peak in  $R_{xx}$  associated with a crossover from hole-like to electron-like behavior (Fig. S4c). These replica points reflect the self-similarity of the fractal Hofstadter energy spectrum.<sup>3,4</sup> We note that at other fields and gate voltages, the behavior in  $R_{xy}$  can be similar but offset from zero, consistent with previous work.<sup>3,4</sup> The gaps at the hexagon centers occur along lines in the

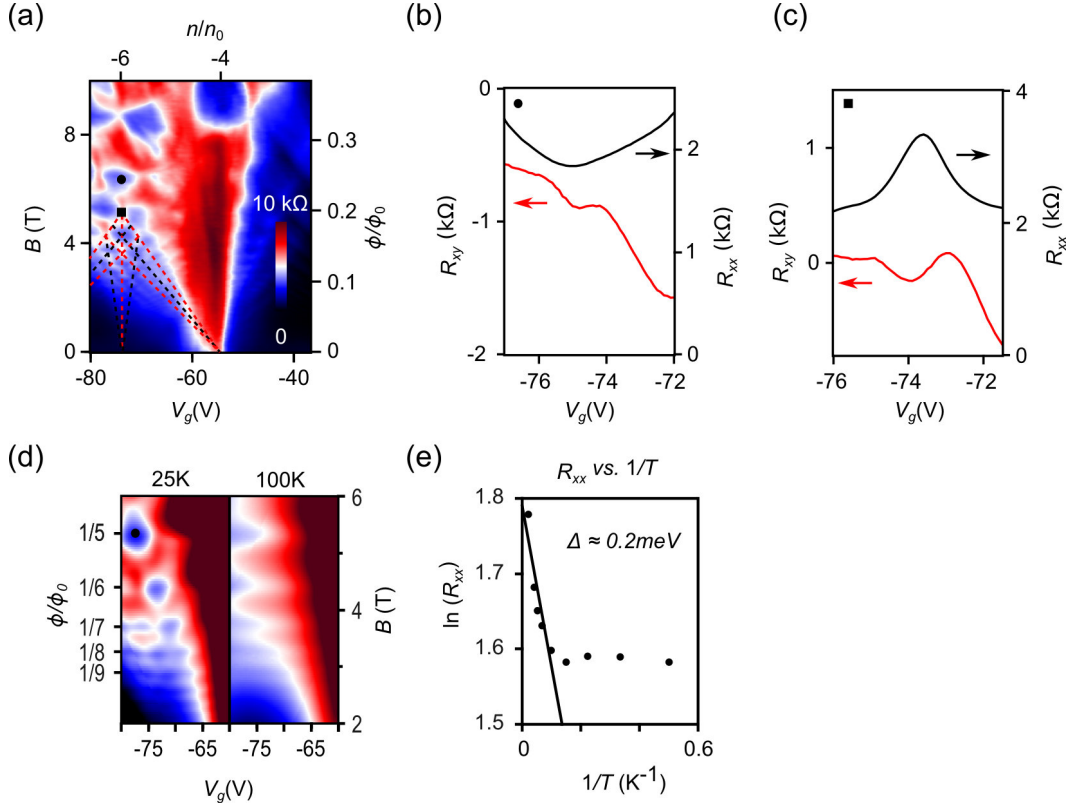


**Figure S4. Replica Dirac points and gaps on hole side.** (a) Color plot of  $R_{xx}$  vs.  $V_g$  (bottom) / normalized density (top) and  $B$  (left axis)/flux quanta per unit moiré superlattice unit cell (right axis) near the sDP on the hole side showing hexagonal ridges for sample G3 with four-terminal mobility  $\sim 20,000$   $cm^2/V\cdot s$ . Dirac points occur along the red dashed lines, while gaps occur along the black dashed lines. A nonlinear color mapping was used to enhance contrast. (b)  $R_{xx}$  (black) and  $R_{xy}$  (red) vs.  $V_g$  taken near the point indicated by the solid circle in (a). (c)  $R_{xx}$  (black) and  $R_{xy}$  (red) vs.  $V_g$  taken near the point indicated by the solid square in (a). (d)  $R_{xx}$  region to the left of the sDP at  $T=25$  K and  $T=100$  K. Dark blue corresponds to 3 k $\Omega$ , and dark red to 9 k $\Omega$ . (e) Arrhenius plot of  $R_{xx}$  at the point indicated by the solid circle in (d).

density-field plot that extrapolate to  $n/n_0 = s = -8, -6,$  and  $-4$ . The slopes of the lines are determined to follow  $t = 4m$ , where  $m \neq 0$  is an integer with a sign determined by the extrapolation point. Calculations show that gaps occurring along lines with such slopes result from inversion symmetry breaking by the hBN layer.<sup>8</sup> Such inversion symmetry breaking may indicate the formation of a commensurate lattice phase.<sup>6</sup> The Dirac points occur along lines extrapolating to

$n/n_0=s=-4$  and  $-8$  with slopes  $t=4m+2$ , for integer  $m$  where the sign depends on  $s$ . No clear dominance of features with  $s=0$  and phase shift is observed in this region, consistent with the calculated spectrum that shows larger gaps at the sBZ boundaries without overshadowing bands.<sup>8</sup> Finally,  $R_{xx}$  in the large hole doping regime vs.  $V_g$  and  $B$  is plotted at two additional temperatures in Fig S4d. The Zak miniband structure persists up to at least 100 K indicating an energy scale at least  $E_Z \sim 10-30$  meV for these features. The temperature dependence data of  $R_{xx}$  within one of the hexagonal gap regions is plotted as an Arrhenius plot in Fig. S4e. Analysis of the linear region of the plot yields a gap  $\sim 0.2$  meV. This value is uncertain due to the relatively small range of data above the saturation region. Moreover, the small value may, for example, reflect transport mechanisms such as variable range hopping. More work is required to determine accurately the gaps in this region.

## S7. Details of phase analysis procedure

To determine the absolute phase of the magnetooscillations in the two electron doped regimes we use the method utilized in refs. 25 and 26 of the main text to measure the absolute magnetooscillation phase. The minima are counted with integer index  $N$  and the maxima with index  $N+1/2$  and plotted versus the value of  $1/B$  for each extremum. The data are fit to a straight line to find the intercept, which reveals the absolute oscillation phase, as done in refs. 25 and 26. However, because of the transition region, the extrema for doping past the sDP cannot readily be counted from a fixed  $1/B$  value. Instead we first count starting from the first oscillation outside the transition region (or the first available oscillation for  $V_g < V_{sDP}$ ), and perform a linear fit to find the period. We then plot the magnetooscillations vs.  $1/B$  in units of the period, which reveals the appropriate starting value of  $N$  counting from  $1/B=0$  directly. The  $N$ th minima ( $N$ th+1/2 maxima) is then plotted vs.  $1/B$ . This is shown in main text Fig. 4 for samples G1 and G2. In both samples for doping below the sDP the intercept is  $1/2$ , showing an unconventional quantum Hall effect with  $\pi$  Berry's phase. For doping beyond sDP, the intercept is zero, showing the additional  $\pi$  Berry phase discussed in the main text.

Finally, for both devices G1 and G2, the region where the oscillation phase makes its transition is near a relative  $\nu=10$ , indicating that the observed behavior originates from the superlattice potential. Also, features to the right of the transition region and those to the left extrapolate back to the same point at  $B=0$ , indicating that the phase shift cannot be accounted for by an offset due to a charge inhomogeneity within the sample. Finally, the analysis in Fig. 4 shows that outside of the transition region the Berry's phase is consistently  $\pi$  in the region below the sDP and consistently  $0 \pmod{2\pi}$  above it, ruling out a magnetic field offset, and also indicating that sample inhomogeneities are not a significant factor in the observed phase shift. Taken together along with the discussion in section S5, this indicates that the observed phase shift behavior does not originate from sample inhomogeneities, or offsets in charge or magnetic field.

## References

1. Zomer, P. J.; Dash, S. P.; Tombros, N.; van Wees, B. J. *Appl. Phys. Lett.* **2011**, *99*, 232104.
2. Hunt, B.; Sanchez-Yamagishi, J. D.; Young, A. F.; Yankowitz, M.; LeRoy, B. J.; Watanabe, K.; Taniguchi, T.; Moon, P.; Koshino, M.; Jarillo-Herrero, P. *Science* **2013**, *340*, 1427-1430.
3. Dean, C. R.; Wang, L.; Maher, P.; Forsythe, C.; Ghahari, F.; Gao, Y.; Katoch, J.; Ishigami, M.; Moon, P.; Koshino, M.; Taniguchi, T.; Watanabe, K.; Shepard, K. L.; Hone, J.; Kim, P. *Nature* **2013**, *497*, 598-602.
4. Ponomarenko, L. A.; Gorbachev, R. V.; Yu, G. L.; Elias, D. C.; Jalil, R.; Patel, A. A.; Mishchenko, A.; Mayorov, A. S.; Woods, C. R.; Wallbank, J. R.; Mucha-Kruczynski, M.; Piot, B. A.; Potemski, M.; Grigorieva, I. V.; Novoselov, K. S.; Guinea, F.; Fal'ko, V. I.; Geim, A. K. *Nature* **2013**, *497*, 594-597.
5. Eckmann, A.; Park, J.; Yang, H.; Elias, D.; Mayorov, A. S.; Yu, G.; Jalil, R.; Novoselov, K. S.; Gorbachev, R. V.; Lazzeri, M. *Nano Lett.* **2013**, *13*, 5242-5246.
6. Woods, C. R.; Britnell, L.; Eckmann, A.; Ma, R. S.; Lu, J. C.; Guo, H. M.; Lin, X.; Yu, G. L.; Cao, Y.; Gorbachev, R. V.; Kretinin, A. V.; Park, J.; Ponomarenko, L. A.; Katsnelson, M. I.; Gornostyrev, Y. N.; Watanabe, K.; Taniguchi, T.; Casiraghi, C.; Gao, H. J.; Geim, A. K.; Novoselov, K. S. *Nat. Phys.* **2014**, *10*, 451-456.
7. Chen, X.; Wallbank, J. R.; Patel, A. A.; Mucha-Kruczyński, M.; McCann, E.; Fal'ko, V. I. *Phys. Rev. B* **2013**, *89*, 075401.
8. Wallbank, J. R.; Patel, A. A.; Mucha-Kruczyński, M.; Geim, A. K.; Fal'ko, V. I. *Phys. Rev. B* **2013**, *87*, 245408.
9. Young, A. F.; Kim, P. *Nat. Phys.* **2009**, *5*, 222-226.
10. Ando, T. *J. Phys. Soc. Jpn.* **2006**, *75*, 074716.
11. Cheianov, V. V.; Fal'ko, V. I. *Phys. Rev. Lett.* **2006**, *97*, 226801.
12. Das Sarma, S.; Adam, S.; Hwang, E. H.; Rossi, E. *Rev. Mod. Phys.* **2011**, *83*, 407-470.